

Article

Fabrication of 3D Hierarchical Spherical Honeycomb-Like $\text{Nd}_2\text{O}_3/\text{Co}_3\text{O}_4/\text{Graphene}/\text{Nickel}$ Foam Composite Electrode Material for High-Performance Supercapacitors

Huihui Liang ¹, Shasha Wang ¹, Shixiang Lu ^{1,*}, Wenguo Xu ¹ and Min Zhou ²¹ School of Chemistry and Chemical Engineering, Beijing Institute of Technology, Beijing 100081, China² School of Chemical Science and Technology, Yunnan University, Kunming 650091, China

* Correspondence: shixianglu@bit.edu.cn; Tel.: +86-10-6891-2667

Abstract: A 3D hierarchical spherical honeycomb-like composite electrode material of neodymium oxide (Nd_2O_3), cobalt tetraoxide (Co_3O_4), and reduced graphene oxide (rGO) on nickel foam (named as $\text{Nd}_2\text{O}_3/\text{Co}_3\text{O}_4/\text{rGO}/\text{NF}$) were successfully fabricated by combining the hydrothermal synthesis method and the annealing process. Nickel foam with a three-dimensional spatial structure was used as the growth substrate without the use of any adhesives. The $\text{Nd}_2\text{O}_3/\text{Co}_3\text{O}_4/\text{rGO}/\text{NF}$ composite has outstanding electrochemical performance and can be used directly as an electrode material for supercapacitors (SCs). By taking advantage of the large specific surface area of the electrode material, it effectively slows down the volume expansion of the active material caused by repeated charging and discharging processes, improves the electrode performance in terms of electrical conductivity, and significantly shortens the electron and ion transport paths. At a 1 A/g current density, the specific capacitance reaches a maximum value of 3359.6 F/g. A specific capacitance of 440.4 F/g with a current density of 0.5 A/g is still possible from the built symmetric SCs. The capacitance retention rate is still 95.7% after 30,000 cycles of testing at a high current density of 10 A/g, and the energy density is 88.1 Wh/kg at a power density of 300 W/kg. The outcomes of the experiment demonstrate the significant potential and opportunity for this composite material to be used as an electrode material for SCs.



Citation: Liang, H.; Wang, S.; Lu, S.; Xu, W.; Zhou, M. Fabrication of 3D Hierarchical Spherical Honeycomb-Like $\text{Nd}_2\text{O}_3/\text{Co}_3\text{O}_4/\text{Graphene}/\text{Nickel}$ Foam Composite Electrode Material for High-Performance Supercapacitors. *Materials* **2023**, *16*, 1694. <https://doi.org/10.3390/ma16041694>

Academic Editors: Michela Alfè, Jung Bin In and Gueorgui Gueorguiev

Received: 10 January 2023

Revised: 2 February 2023

Accepted: 14 February 2023

Published: 17 February 2023



Copyright: © 2023 by the authors. Licensee MDPI, Basel, Switzerland. This article is an open access article distributed under the terms and conditions of the Creative Commons Attribution (CC BY) license (<https://creativecommons.org/licenses/by/4.0/>).

Keywords: graphene; Nd_2O_3 ; Co_3O_4 ; nickel foam; supercapacitor

1. Introduction

With the development of the economy and society, people's dependence on energy has been increasing since about the Industrial Revolution. These energy sources cannot be separated from the extraction and consumption of fossil fuels [1,2], and it is sure to happen that rapid economic development has brought serious environmental pollution at the same time [3,4]. However, as sustainable energy sources such as wind and solar are easily impacted by location and time, urgent research and development into novel energy storage technologies are required [5]. Supercapacitors (SCs) are energy storage devices that outperform batteries in terms of lifecycle, speed of charging and discharging, power, safety, non-toxicity, and cleanliness [6]. The current aim of SC research is to increase the energy density and capacitance of the materials utilized [7,8]. According to their methodology of pumped storage, SCs can be split into double-layer capacitors, pseudocapacitor capacitors, and hybrid capacitors. The portion of charge storage capacity of the double-layer capacitors is based primarily on the electrode material's capacity to absorb ions on the surface [9,10]. The charge storage method in pseudocapacitors is accomplished via a quick and reversible Faraday redox reaction between the electrode material on the electrode surface and the ions in the electrolyte. As a result, the large specific surface area of the electrode material surface structure can also more effectively provide ions to the electrode. Both of these procedures result in the charge storage principle of hybrid SC.

Multi-component metal sulfides and oxides are the most prevalent pseudocapacitive electrode materials because they can generate both double-layer capacitance and pseudocapacitance through electrochemical processes during the charge storage process [11]. The successful fabrication of such electrode materials opens up a whole new horizon for electrode materials for SCs, not only by modifying the ratio between different metal elements to seek greater potential window, conductivity, and other aspects of electrode materials, but also by thinking about compounding with other carbon-based materials to make full use of the synergy between different materials, to complement each other's strengths, and to build electrode materials for SCs that are more robust and durable [12,13]. Researchers recently created brand-new electrode materials from inorganic rare-earth elements in an effort to better the electrochemical properties of electrode materials [14]. Rare earth elements are highly valued for their exceptional physicochemical qualities, which are derived from their unique 4f electron configuration and used in optics, catalysts, and energy devices [15,16]. LaFeO₃ (LF) chalcogenides were created by doping Mn and Nd during hydrothermal synthesis to produce La_{0.8}Nd_{0.2}Fe_{0.8}Mn_{0.2} (LNFM) [17]. When the scan rate was 50 mV/s, the specific capacitance of the electrode could still reach 158 F/g, which was much higher than that of the pure LF sample and the single-doped LF. The capacity retention of the composite material was also discovered to be 92.4% at 10,000 cycles (85.37% for the LNFM sample) during the research on the cycling stability of the electrode material. Additionally, research has shown that doping cobalt trioxide with rare-earth-based elements such as lanthanum, neodymium, gadolinium, and samarium improved the performance of the materials to varying degrees. Rare earth elements were discovered to be involved in lowering charge transfer resistance during doping, and this structural defect caused by doping can be seen clearly by scanning electron microscope (SEM) while also shortening the path that electrolyte ions take during diffusion [18]. Still, there are not many studies on the use of lanthanide rare earth metals in SCs.

Here, Nd₂O₃/Co₃O₄/reduced graphene oxide (rGO) with a three-dimensional porous honeycomb spherical structure with a high specific surface area of 107.6246 m²/g and an average pore size of about 12 nm were successfully prepared experimentally using a simple one-step hydrothermal synthesis and annealing. When the Nd₂O₃/Co₃O₄/rGO/NF composite electrode was implemented as the electrode material with a current density of 1 A/g, its specific capacitance was 3359.6 F/g. In addition, the prepared electrodes can be directly assembled into symmetrical SCs with a specific capacitance of 440.4 F/g at a capacitance density of 0.5 A/g and a capacitance retention rate of 95.7% (30,000 cycles) even at a high current density of 10 A/g, making Nd₂O₃/Co₃O₄/rGO/NF an SC electrode material with great application prospects.

2. Materials and Methods

2.1. Materials

The original graphite powder, concentrated HCl (36%), concentrated H₂SO₄ (98%), concentrated KMnO₄ (99%), ethanol (99.3%), hydrogen peroxide (30%wt), acetone (99.6%), and potassium hydroxide (KOH) were all purchased from Beijing Fine Chemicals Co. Ltd. (Beijing, China) Nickel foam (NF) is made available by Kunshan Tonghui Electronic Technology Co. Ltd. (Kunshan, China) Shanghai Maclean Biochemical Co. Ltd. (Shanghai, China) prepared urea (CH₄N₂O), cobalt nitrate hexahydrate (Co(NO₃)₂·6H₂O), and neodymium acetate pentahydrate (Nd(CH₃COO)₃·5H₂O). All of the chemical reagents used in the experiments were analytically pure and employed in accordance with the set usage guidelines.

2.2. Preparation of Nd₂O₃/Co₃O₄/rGO/NF Composite Electrode

2.2.1. Pretreatment of Conductive Substrate NF

The NFs (20 mm × 10 mm × 1 mm) were manually cut beforehand, washed with acetone, ethanol, and deionized water in turn for 30 min in an ultrasonic water bath, and then dried in an oven at 60 °C for 12 h to get rid of any potential contaminants.

2.2.2. Synthesis of $\text{Nd}_2\text{O}_3/\text{Co}_3\text{O}_4/\text{rGO}/\text{NF}$ Precursors

The GO used in the experiments was obtained by using graphite powder as raw material and prepared by using the modified Hummer method [19]. A total of 0.6 mmol (0.175 g) $\text{Co}(\text{NO}_3)_2 \cdot 6\text{H}_2\text{O}$, 0.6 mmol (0.247 g) $\text{Nd}(\text{CH}_3\text{COO})_3 \cdot 5\text{H}_2\text{O}$ and 1 mmol (0.060 g) urea were added to 7.5 mL deionized water to dissolve it fully and then continued to stir magnetically for 40 min, then add 7.5 mL 2 mg/mL GO homogeneous suspension that has been sonicated for 2 h and continue to stir by magnetic force for 40 min to ensure that the black solution A is mixed well. In a volume of 25 mL PTFE-lined reactor, the pretreated nickel foam was mixed with solution A and placed in an oven for 12 h at 140 °C. Then it was rinsed several times with deionized water and anhydrous ethanol and dried in the oven (90 °C, 4 h), and set aside.

2.2.3. Synthesis of $\text{Nd}_2\text{O}_3/\text{Co}_3\text{O}_4/\text{rGO}/\text{NF}$

The precursor samples prepared above were calcined in a muffle furnace, and annealed at 250 °C for 2 h. After cooling to room temperature, the surface of NF was observed to change from light purple to black, and the composite electrode of $\text{Nd}_2\text{O}_3/\text{Co}_3\text{O}_4/\text{rGO}/\text{NF}$ and $\text{Nd}_2\text{O}_3/\text{Co}_3\text{O}_4/\text{rGO}$ was obtained with an average mass of $1.50 \pm 0.11 \text{ mg}/\text{cm}^2$ loaded on NF. The $\text{Co}_3\text{O}_4/\text{rGO}/\text{NF}$ composite electrode was synthesized as shown in Figure 1. The experimental procedures for the preparation of $\text{Nd}_2\text{O}_3/\text{Co}_3\text{O}_4/\text{rGO}$, $\text{Nd}_2\text{O}_3/\text{rGO}/\text{NF}$, $\text{Co}_3\text{O}_4/\text{rGO}/\text{NF}$ and rGO/NF are shown in supplementary S1–S4.

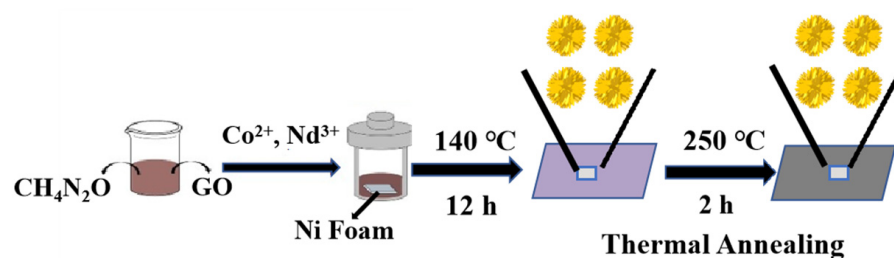


Figure 1. The preparation process of $\text{Nd}_2\text{O}_3/\text{Co}_3\text{O}_4/\text{rGO}/\text{NF}$ composite electrode.

2.3. Structural Characterization

The constituent structures of the materials were characterized and analyzed by an x-ray electron spectrometer (XPS, model PHI 5300, Physical Electronics, Chanhassen, MN, USA) and a Bruker D8 Advance x-ray powder diffractometer (XRD, $2\theta = 10^\circ \sim 80^\circ$) equipped with Cu K_α ($\lambda = 0.15418 \text{ nm}$). The surface morphological structure of the sample materials was visualized using a scanning electron microscope (SEM, Quanta 600, FEI, Rock Hill, SC, USA) with its own energy spectrometer (EDS, Oxford, Gemini 300), a high-resolution transmission electron microscope (HRTEM) and a transmission electron microscope (TEM, JEM-2100, JEOL, Tokyo, Japan). A Renishaw InVia confocal Raman spectrometer, a Leica DMLM microscope, and an argon ion laser (514.5 nm, model Stellar-REN, Modu-Laser, Centerville, UT, USA) as the excitation source were used to capture the Raman spectra.

2.4. Electrochemical Characterization

The produced electrodes were electrochemically tested on an electrochemical workstation (CHI 760E, CH Instruments, Bee Cave, TX, USA) using a standard three-electrode system and a potassium hydroxide solution at a concentration of 6 mol/L as the electrolyte. The prepared electrode served as the working electrode during the test, with the saturated calomel electrode serving as the reference electrode and the platinum electrode performing as the counter electrode.

2.4.1. Cyclic Voltammetry (CV)

To illustrate the variation in electrochemical performance between various electrodes, the CV curves of various sample electrodes were measured and compared. The charge

(capacity, in C/g) can be calculated could be calculated from the CV curves, using the following Equation (1) [20].

$$C = \frac{1}{Evm} \int_{V_1}^{V_2} idV \quad (1)$$

where E is the potential window in this equation ($E = V_2 - V_1$, where V_2 and V_1 are the potential window's edges), v is the scan rate, i is the discharge (or charge) current, and dV is the infinitesimal potential change.

2.4.2. Constant Current Charge and Discharge (GCD)

The specific capacitance of the corresponding electrodes was determined by measuring and comparing the GCD curves of various sample electrodes at current densities of 1~10 A/g and voltage windows of $-0.1\sim 0.4$ V. The specific capacitance of the three-electrode system can also be calculated and is listed in Equation (2) [21].

$$C = \frac{(I \times \Delta t)}{(m \times \Delta V)} \quad (2)$$

Equation (3) is used to determine the energy density of the electrodes (E, Wh/kg) and Equation (4) is used to determine the power density (P, W/kg) in order to define the symmetric SC [22].

$$E = \frac{(C \times \Delta V^2)}{(2 \times 3.6)} \quad (3)$$

$$P = \frac{(3600 \times E)}{\Delta t} \quad (4)$$

where C stands for the specific capacitance of electrode, I exemplifies the constant discharge current, t exemplifies the discharge time, m exemplifies the mass of the active material on the electrode, and V (V) exemplifies the total voltage window.

2.4.3. Electrochemical Impedance Spectroscopy (EIS)

With the use of EIS, the electrode interfacial resistance and mass transfer resistance are qualitatively assessed, and the causes of the enhanced electrochemical performance are looked into.

At open circuit voltage amplitude of 5 mV, EIS is measured in the frequency range of 100 kHz to 0.01 Hz.

2.4.4. Test of Cycling Stability

Using a constant current charge/discharge cycle test, the electrochemical stability of the $\text{Nd}_2\text{O}_3/\text{Co}_3\text{O}_4/\text{rGO}/\text{NF}$ composite electrode was assessed in this study. The outstanding electrochemical performance and cycling stability of the composite electrode were confirmed after 30,000 cycles of the stability test.

3. Results and Discussion

3.1. Analyses of Morphology and Structure

The produced material was measured and examined using XPS in the scanning range of 0~1000 V in order to investigate and describe the elemental composition and chemical state of the material. In the necessary scanning range, it was uncovered that four elements, Nd, Co, C, and O, were for certain as shown in Figure 2a. The presence of three peaks can be seen in the C1s high-resolution spectrum as shown in Figure 2b, with the strongest peak at 284.8 eV indicating the presence of C-C bonds and the other relatively weak peaks at 285.3 eV and 289.2 eV indicating the presence of C-O and C=O bonds, respectively. It can be inferred from the foregoing analysis that GO was successfully reduced in the experiment. Additionally, the high-resolution O1s spectra as shown in Figure 2e demonstrate that the peak at 529.6 eV is associated with the presence of the Co-O bond in the material [23], the peak at 531.6 eV is attributable to lattice oxygen (Nd/O bond) [24], and the remaining peak

at 530.8 eV is linked to the material capability to adsorb oxygen molecules [25]. Various positions of peaks can be seen in the high-resolution spectrum of the element Co, where the peak positions at 780.1 eV and 795.3 eV correspond to the typical peaks of $\text{Co}2p_{3/2}$ and $\text{Co}2p_{1/2}$ of Co_3O_4 in the material, respectively, as shown in Figure 2c. Additionally, it can be seen that the $\text{Co}2p_{3/2}$ peak has a satellite peak at 781.8.5 eV/780.1 eV and the $\text{Co}2p_{1/2}$ peak has a satellite peak at 796.7 eV/795.3 eV, indicating that there is a simultaneous presence of Co^{2+} and Co^{3+} in the material [26]. The magnitude of the binding energy difference between the two peak positions is about 15.2 eV. This phenomenon indicates the presence of Co(II)/Co(III) in the sample. The high-resolution XPS pattern of $\text{Nd}3d$ in the image as shown in Figure 2d has two distinct peaks at 982.3 eV and 1001.4 eV [27], which are caused by the spin splitting of $\text{Nd}3d$ orbitals into $\text{Nd}3d_{5/2}$ and $\text{Nd}3d_{3/2}$ orbitals with an energy difference of 19.1 eV [28]. This is evidence that Nd_2O_3 was successfully prepared for the experiment.

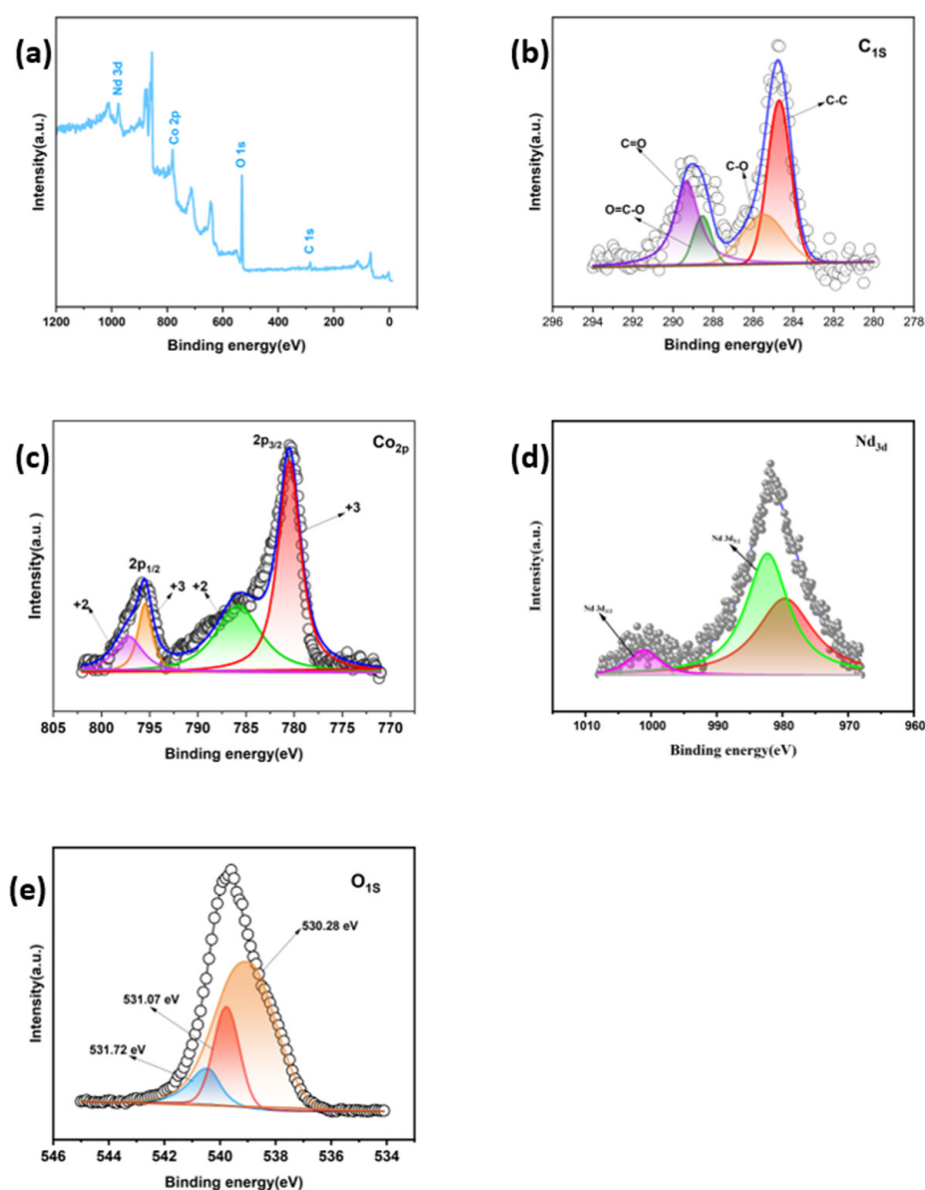


Figure 2. (a) XPS spectra of the $\text{Nd}_2\text{O}_3/\text{Co}_3\text{O}_4/\text{rGO}$ composite electrode material; High-resolution XPS spectra of (b) $\text{C}1s$; (c) $\text{Co}2p$; (d) $\text{Nd}3d$; and (e) $\text{O}1s$ of the $\text{Nd}_2\text{O}_3/\text{Co}_3\text{O}_4/\text{rGO}$ composite electrode material.

X-ray energy spectrometry (EDS) was used to identify the elemental makeup of the $\text{Nd}_2\text{O}_3/\text{Co}_3\text{O}_4/\text{rGO}/\text{NF}$ composite electrode. There is no doubt that the manufactured composite electrode material is made up of the five components, O, C, Co, Ni, and Nd, as indicated in Figure 3. EDS spectroscopy can be used to estimate the required ratio of each element on the surface of the composite electrode material. The mass percentages of Co and Nd are 19.64% and 0.38%, respectively. Element C corresponds to the presence of graphene in the material, while elements Nd and Co correspond to the presence of Nd_2O_3 and Co_3O_4 , respectively, which were successfully prepared and loaded onto the surface of graphene. This result provides a more precise confirmation that the NF substrate has been successfully loaded with Nd_2O_3 and Co_3O_4 . Additionally, elemental mapping analysis can be used to investigate the elemental distribution in $\text{Nd}_2\text{O}_3/\text{Co}_3\text{O}_4/\text{rGO}/\text{NF}$. The elements, C, O, Co, Ni, and Nd, had a homogeneous distribution on the electrode, as illustrated in Figure S1, and there were no impurities observed.

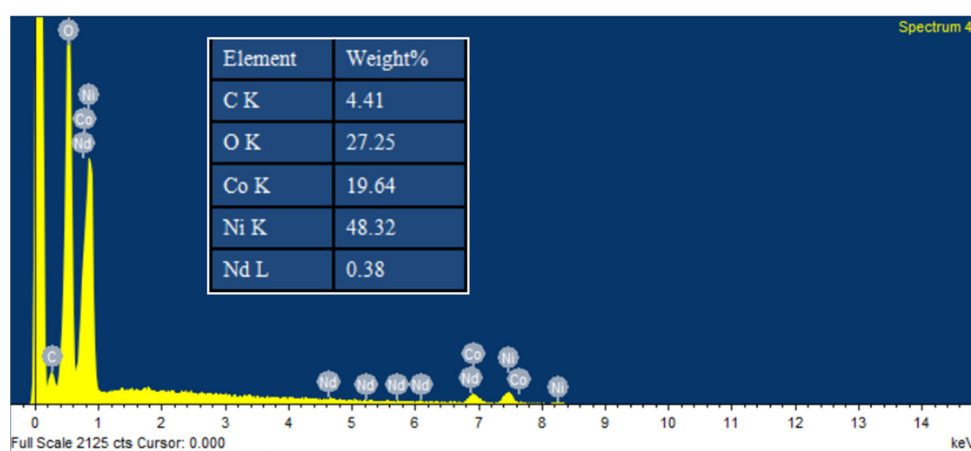


Figure 3. EDS of $\text{Nd}_2\text{O}_3/\text{Co}_3\text{O}_4/\text{rGO}/\text{NF}$.

Scanning electron microscopy was utilized to investigate the prepared electrode in order to describe the surface morphology and structure in greater detail. Figure 4a–f shows the bare NF, rGO/NF, $\text{Nd}_2\text{O}_3/\text{rGO}/\text{NF}$, $\text{Co}_3\text{O}_4/\text{rGO}/\text{NF}$, $\text{Nd}_2\text{O}_3/\text{Co}_3\text{O}_4/\text{NF}$, and $\text{Nd}_2\text{O}_3/\text{Co}_3\text{O}_4/\text{rGO}/\text{NF}$ SEM images. Figure 4a makes it evident that the treated NF with a smooth surface simultaneously conveys a three-dimensional skeleton structure. After being loaded with rGO, the NF surface that had previously displayed a smooth state becomes rough, and it can be seen that visible ripple-like folds, as well as a significant number of cracks, emerge on the material surface [29], as shown in Figure 4b. In this instance, the rough surface helps with ion diffusion and transport, which significantly lowers ion transport resistance and speeds up ion movement. As illustrated in Figure 4c, cracks can be visible. On the NF, the monometallic Nd_2O_3 forms a network of crossing and tightly connected nanofibers, and these dense networks are less conducive to the entry of electrolytes during the electrode reaction, limiting the interaction between the electrolyte and active sites. Additionally, as demonstrated in Figure 4d, the monometallic Co_3O_4 results in a significant amount of nanoneedle-like structures on NF. The scanning electron microscopy image of $\text{Nd}_2\text{O}_3/\text{Co}_3\text{O}_4/\text{NF}$ is shown in Figure 4e, and it can be seen that there are many 3D hierarchical honeycomb-like structures. The honeycomb-like structures create a sparse mesh with greater pore sizes and larger specific surface areas between each other. These honeycomb-like structures are formed of many nanowires and nanofibers together, and they have the propensity to expand upward. Nd_2O_3 and Co_3O_4 are deposited on NF during hydrothermal synthesis, creating porous spherical honeycomb-like structures when graphene is added to the composite. These 3D hierarchical spherical honeycomb structures as shown in Figure 4f facilitate the contact between the electrode material and the electrolyte solution and increase the specific surface area of the electrode material, which raises the active sites, lowers the ion transport resistance, and shortens the ion diffusion path [30].

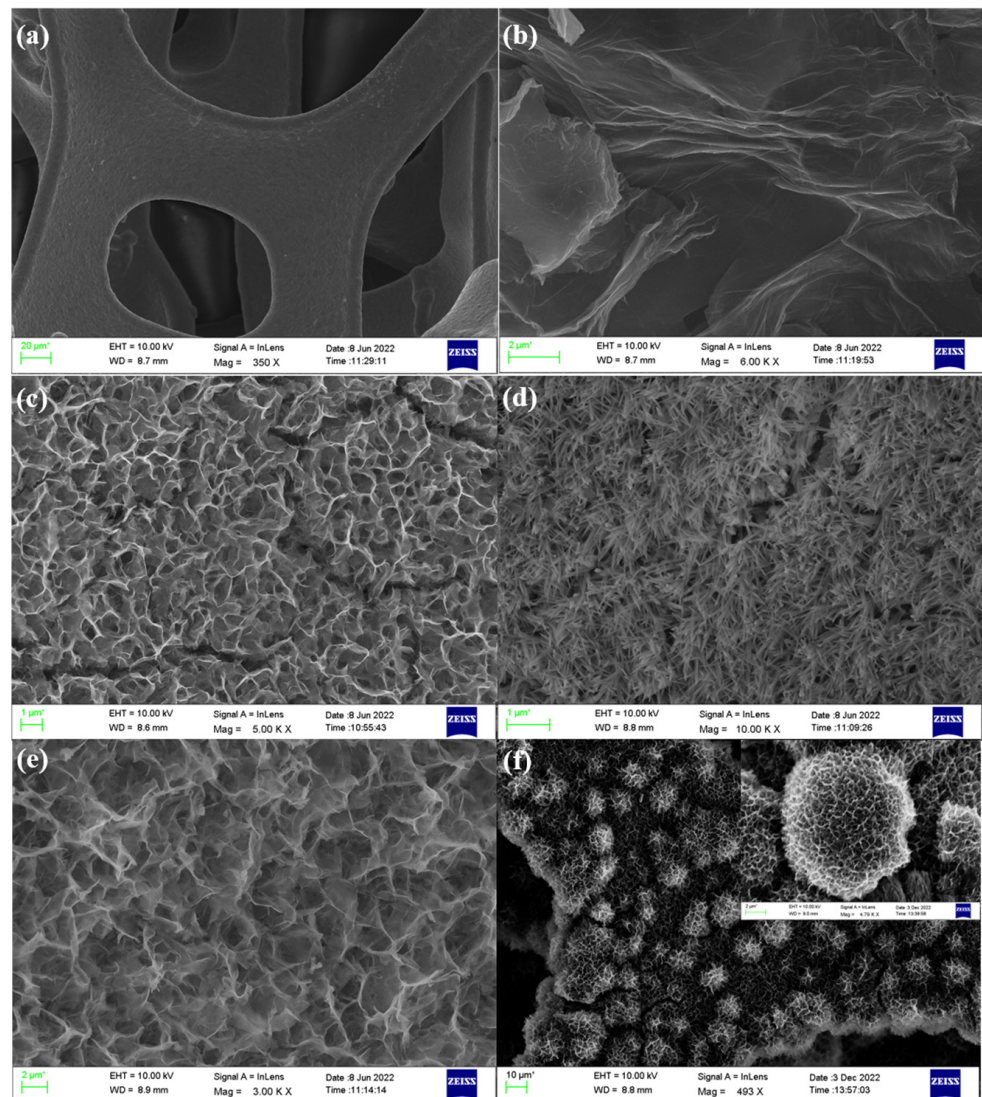


Figure 4. SEM images of (a) bare NF, (b) rGO/NF, (c) $\text{Nd}_2\text{O}_3/\text{rGO}/\text{NF}$, (d) $\text{Co}_3\text{O}_4/\text{rGO}/\text{NF}$, (e) $\text{Nd}_2\text{O}_3/\text{Co}_3\text{O}_4/\text{NF}$, and (f) $\text{Nd}_2\text{O}_3/\text{Co}_3\text{O}_4/\text{rGO}/\text{NF}$; the inset in (f) is the plot of $\text{Nd}_2\text{O}_3/\text{Co}_3\text{O}_4/\text{rGO}/\text{NF}$ magnification.

By comparing the Raman curves of the materials $\text{Nd}_2\text{O}_3/\text{Co}_3\text{O}_4/\text{rGO}$, $\text{Nd}_2\text{O}_3/\text{Co}_3\text{O}_4$ and GO, Raman spectroscopy is able to qualitatively determine if GO has been successfully reduced in the material. The Raman spectra of GO, $\text{Nd}_2\text{O}_3/\text{Co}_3\text{O}_4/\text{NF}$, and $\text{Nd}_2\text{O}_3/\text{Co}_3\text{O}_4/\text{rGO}/\text{NF}$ electrode materials are depicted in Figure 5a. Both GO and $\text{Nd}_2\text{O}_3/\text{Co}_3\text{O}_4/\text{rGO}/\text{NF}$ have Raman spectra that show the G-band at 1582 cm^{-1} and the D-band at 1344 cm^{-1} , which are formed by the stretching vibrations of sp^2 - and sp^3 -hybridized carbon atoms in graphite, respectively [31,32]. It is customary to utilize the ratio of D-band to G-band peak intensities (I_D/I_G) to indicate the structural flaws in graphene and the extent of graphene reduction. Graphene structural flaws and the level of graphene reduction are frequently represented by the ratio of D-band to G-band peak intensities (I_D/I_G) [33]. In general, a higher I_D/I_G ratio indicates a larger structural flaw in the material, in this experiment, it is indicated that a larger reduction in the GO, which was effectively transformed to rGO. $\text{Nd}_2\text{O}_3/\text{Co}_3\text{O}_4/\text{rGO}$ has a higher I_D/I_G value than rGO (0.98), which is 1.14. The Raman spectra of $\text{Nd}_2\text{O}_3/\text{Co}_3\text{O}_4$ and $\text{Nd}_2\text{O}_3/\text{Co}_3\text{O}_4/\text{rGO}$ also show the presence of two additional vibrational modes [34], designated as F_{2g} and A_{1g} , respectively. The band at 502 cm^{-1} corresponds to the F_{2g} of Co_3O_4 , whereas the weak

spectral band of A_{1g} at 651 cm^{-1} is assumed to be connected to the properties of the octahedral lattice positions inhabited by Co^{3+} . As indicated in Figure 5a, the moderately intense $F_g + E_g$ Raman band at 320.5 cm^{-1} was also discovered. In conclusion, the $\text{Nd}_2\text{O}_3/\text{Co}_3\text{O}_4/\text{NF}$ electrode materials were successfully prepared, as evidenced by the Raman characteristic peaks of both Nd_2O_3 and Co_3O_4 visible in the $\text{Nd}_2\text{O}_3/\text{Co}_3\text{O}_4/\text{NF}$ material. The aforementioned phenomena and results also support this conclusion. Due to the porous honeycomb spherical structure of the manufactured $\text{Nd}_2\text{O}_3/\text{Co}_3\text{O}_4/\text{rGO}$ material, it is assumed to have a large specific surface area. Thus, the nitrogen adsorption-desorption method was applied to analyze the material's properties in order to determine the specific surface area and pore size distribution. As depicted in Figure 5b, a noticeable H3-type hysteresis loop appears on the curve at higher relative pressure, reflecting a classic IV-type isotherm feature [35]. According to the test results, the $\text{Nd}_2\text{O}_3/\text{Co}_3\text{O}_4/\text{rGO}$ composite has a large specific surface area of $107.6246\text{ m}^2/\text{g}$, which makes it advantageous to yield abundant redox sites for Faraday energy storage when redox processes occur. The $\text{Nd}_2\text{O}_3/\text{Co}_3\text{O}_4/\text{rGO}$ material is rich in mesopores, with mesopore size largely concentrated between 3 nm – 4 nm , as illustrated by the inset, which reveals the pore size distribution with an average pore size of about 12 nm .

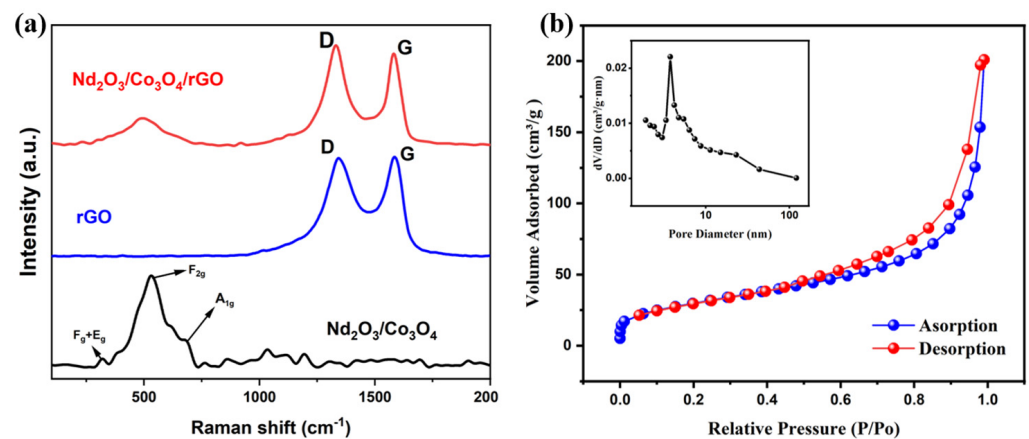


Figure 5. (a) Raman spectra of $\text{Nd}_2\text{O}_3/\text{Co}_3\text{O}_4/\text{rGO}/\text{NF}$; (b) Nitrogen adsorption and desorption isotherm of $\text{Nd}_2\text{O}_3/\text{Co}_3\text{O}_4/\text{rGO}$ with the pore size distribution in the insets.

The constituent phases of $\text{Nd}_2\text{O}_3/\text{Co}_3\text{O}_4/\text{rGO}/\text{NF}$ were characterized by XRD as shown in Figure 6a. The characteristic peaks of metallic nickel, which correspond to the (111), (200), and (220) crystal planes of metallic nickel, are positioned at 44.3° , 51.7° , and 76.2° , respectively. These predominant peaks are easily noticeable in the image (JCPDS card No. 04-0850). Additionally, the (220), (311), and (422) crystallographic planes of Co_3O_4 are represented by 31.3° , 36.9° , and 55.66° in the curve respectively, going to describe the forming of cubic- Co_3O_4 (JCPDS card No. 42-1467) [36]. The typical Nd_2O_3 peaks at 2θ equal to 28.6° , 40.9° , and 59.2° in Figure 6a all correspond to the (110), (200), and (220) crystal planes of cubic- Nd_2O_3 (JCPDS card No. 83-1356) and the decreased strength of the characteristic Nd_2O_3 peak is thought to be due to the smaller grain size. The absence of the characteristic GO peaks in the spectrum may be induced by the effective separation of GO nanosheets by Nd_2O_3 and Co_3O_4 , which leads to highly disordered dispersion in $\text{Nd}_2\text{O}_3/\text{Co}_3\text{O}_4/\text{rGO}/\text{NF}$ composites and increased specific capacitance [37].

The morphological structure of $\text{Nd}_2\text{O}_3/\text{Co}_3\text{O}_4/\text{rGO}/\text{NF}$ was further inspected and demonstrated as shown in Figure 6 using transmission electron microscopy (TEM), selected area electron diffraction (SAED), and high-resolution transmission electron microscopy (HRTEM). Figure 6b clearly shows a spherical honeycomb-like structure composed of a large number of nanoparticles, which is consistent with the results presented by porous nanospheres in SEM images. With channels for their diffusion and a spherical honeycomb-like structure, the material electron and ion transport rates are greatly increased, which

speeds up the redox reaction during charging and discharging. As a result of measuring HRTEM pictures of $\text{Nd}_2\text{O}_3/\text{Co}_3\text{O}_4/\text{rGO}/\text{NF}$ shown in Figure 6c, distinct lattice stripes with lattice spacings of 0.221 nm, 0.156 nm, and 0.312 nm, which correspond to the (200), (220), and (110) crystal planes of Nd_2O_3 (JCPDS card No. 83-1356), were obtained. The (311) crystal plane of Co_3O_4 (JCPDS card No. 42-1467) is represented by the lattice spacing of $d = 0.4$ nm. This is consistent with the XRD test results that were reported. As further evidence of the material polycrystalline structures, Figure 6d also displays a selected area electron diffraction pattern, which displays a sequence of concentric diffraction rings.

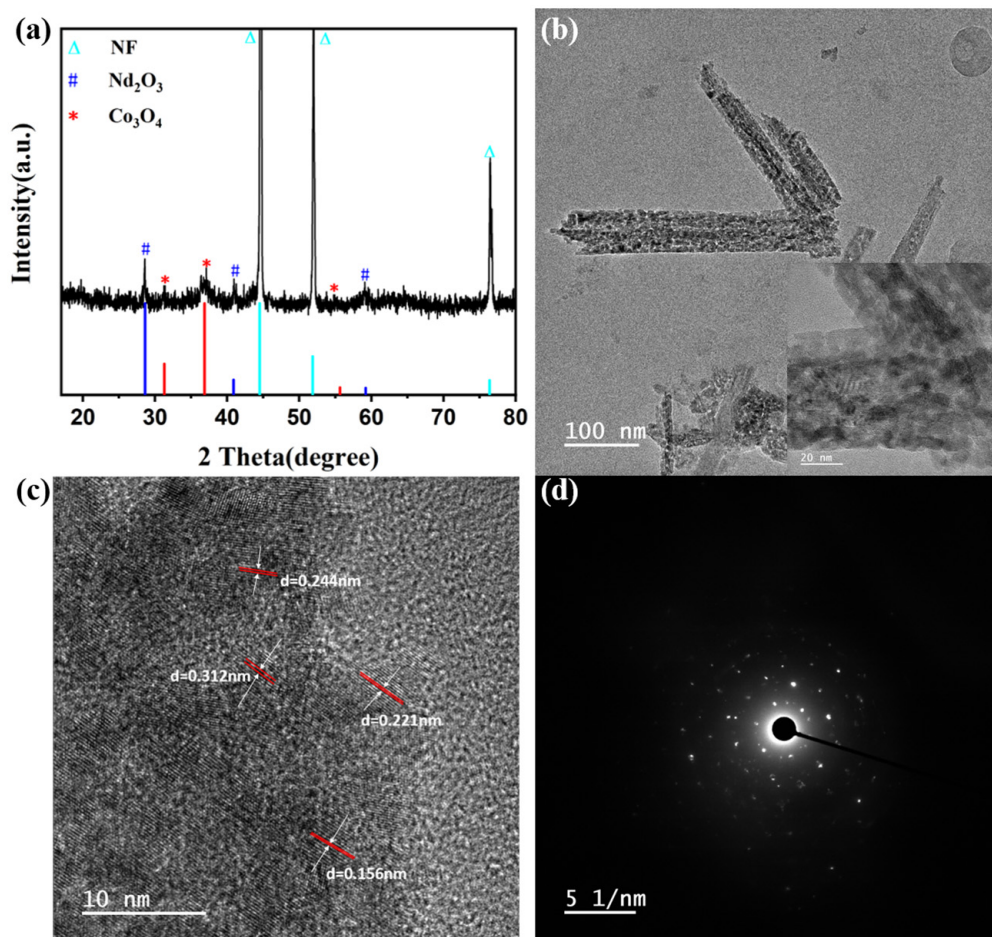


Figure 6. (a) TEM of $\text{Nd}_2\text{O}_3/\text{Co}_3\text{O}_4/\text{rGO}/\text{NF}$; the inset of (a) is the magnified view of nanosheet; (b) HRTEM image; (c) SEAD pattern of $\text{Nd}_2\text{O}_3/\text{Co}_3\text{O}_4/\text{rGO}/\text{NF}$ and (d) XRD of $\text{Nd}_2\text{O}_3/\text{Co}_3\text{O}_4/\text{rGO}/\text{NF}$.

3.2. Electrochemical Properties

The cyclic voltammetry, constant current charge/discharge, and electrochemical impedance spectroscopy at an electrochemical workstation are used to examine the electrochemical performance of the produced electrode $\text{Nd}_2\text{O}_3/\text{Co}_3\text{O}_4/\text{rGO}$ further. All electrochemical characterizations in the typical three-electrode test are carried out with the test ambient environment being a 6 mol/L KOH solution. As demonstrated in Figure 7a, the CV images of the $\text{Nd}_2\text{O}_3/\text{Co}_3\text{O}_4/\text{rGO}/\text{NF}$ electrode at 0.7 V (−0.2 V to −0.5 V) at various scan rates (5 to 100 mV/s) are also depicted. The value of the electrode-specific capacity can be calculated by integrating the CV curve as shown in Figure 7a according to Equation (1). When the scan rates are 5, 25, 50, 75, and 100 mV/s, the magnitudes of the specific capacity of the corresponding $\text{Nd}_2\text{O}_3/\text{Co}_3\text{O}_4/\text{rGO}/\text{NF}$ electrodes are 2272.2, 1550.6, 1185.1, 961.2, and 800.5 C/g, respectively.

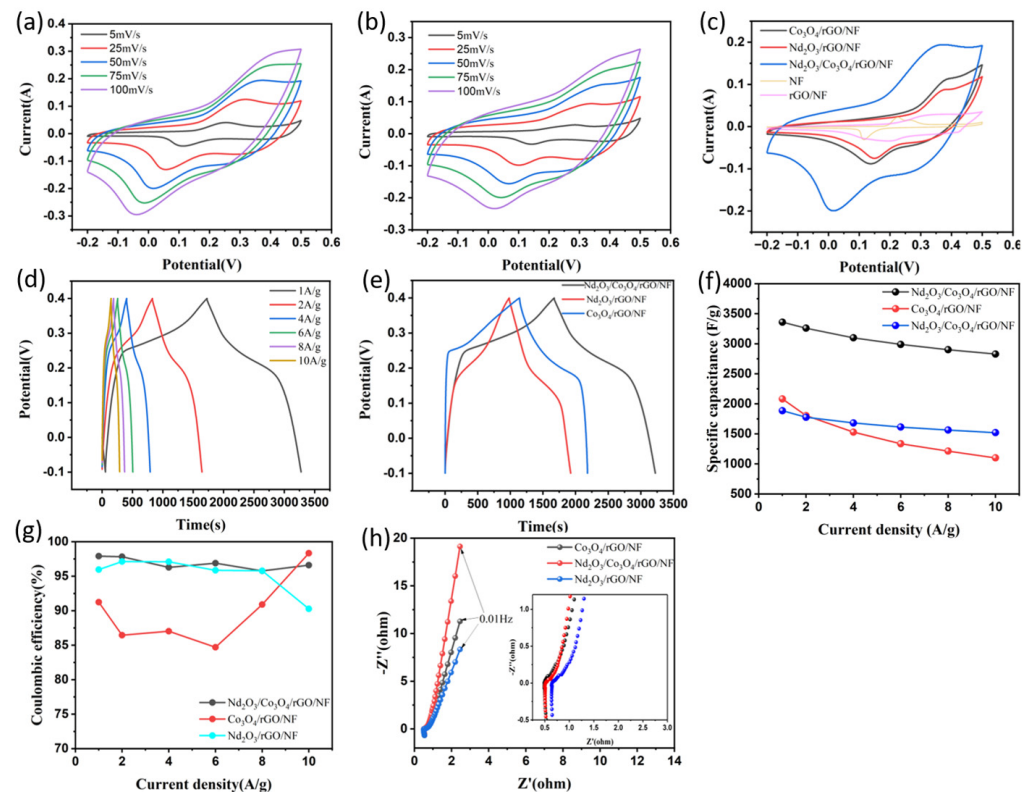
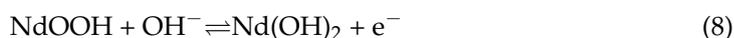
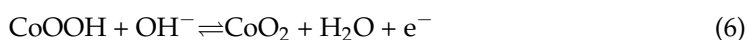


Figure 7. (a,b) CV curves of $\text{Nd}_2\text{O}_3/\text{Co}_3\text{O}_4/\text{rGO}/\text{NF}$ and $\text{Nd}_2\text{O}_3/\text{Co}_3\text{O}_4/\text{NF}$ electrodes under different scan rates; (c) comparison CV curves of $\text{Nd}_2\text{O}_3/\text{Co}_3\text{O}_4/\text{rGO}/\text{NF}$, $\text{Nd}_2\text{O}_3/\text{rGO}/\text{NF}$, $\text{Co}_3\text{O}_4/\text{rGO}/\text{NF}$, rGO/NF and NF electrodes at 50 mV/s ; (d) GCD curves of $\text{Nd}_2\text{O}_3/\text{Co}_3\text{O}_4/\text{rGO}/\text{NF}$ electrodes at different current densities; (e) comparison GCD curves of $\text{Nd}_2\text{O}_3/\text{Co}_3\text{O}_4/\text{rGO}/\text{NF}$, $\text{Nd}_2\text{O}_3/\text{rGO}/\text{NF}$ and $\text{Co}_3\text{O}_4/\text{rGO}/\text{NF}$ electrodes at 1 A/g ; (f) specific capacitances of $\text{Nd}_2\text{O}_3/\text{Co}_3\text{O}_4/\text{rGO}/\text{NF}$, $\text{Nd}_2\text{O}_3/\text{rGO}/\text{NF}$ and $\text{Co}_3\text{O}_4/\text{rGO}/\text{NF}$ electrodes at different current densities; (g) the Coulombic efficiencies of $\text{Nd}_2\text{O}_3/\text{Co}_3\text{O}_4/\text{rGO}/\text{NF}$, $\text{Nd}_2\text{O}_3/\text{rGO}/\text{NF}$ and $\text{Co}_3\text{O}_4/\text{rGO}/\text{NF}$ at different current densities; (h) the Nyquist plots of $\text{Nd}_2\text{O}_3/\text{Co}_3\text{O}_4/\text{rGO}/\text{NF}$, $\text{Nd}_2\text{O}_3/\text{rGO}/\text{NF}$ and $\text{Co}_3\text{O}_4/\text{rGO}/\text{NF}$ electrodes, the circuit inset is the high-frequency region. All of the electrochemical measurements described above were performed in a 6 mol/L KOH solution.

The existence of redox peaks in the scan curves can still be seen clearly at a scan rate of 100 mV/s , and redox peaks can also be seen in all CV curves. This event demonstrates that the electrode material is employed to store charge through a Faraday redox reaction, which in turn supports and demonstrates the material effective use as a pseudocapacitor [38] (the magnitude of the specific capacitance is proportional to the current density). The CV curves of $\text{Nd}_2\text{O}_3/\text{Co}_3\text{O}_4/\text{rGO}/\text{NF}$, $\text{Nd}_2\text{O}_3/\text{rGO}/\text{NF}$, $\text{Co}_3\text{O}_4/\text{rGO}/\text{NF}$, rGO/NF and NF are displayed in Figure 7c at a scan rate of 50 mV/s . In contrast, it is clear that $\text{Nd}_2\text{O}_3/\text{Co}_3\text{O}_4/\text{rGO}/\text{NF}$ has a larger integral area of the CV curve than do $\text{Nd}_2\text{O}_3/\text{rGO}/\text{NF}$ and $\text{Co}_3\text{O}_4/\text{rGO}/\text{NF}$, proving that the material has a higher specific capacitance. The rGO/NF CV curves are subrectangular generally and do not exhibit more pronounced redox peaks, which are indicative of double-layer capacitance properties. Comparatively, the area created by the CV curve is found to be substantially bigger than that of NF , showing that the reduced graphene oxide also provides a small amount of capacitance. As Figure 7a demonstrated, the general shape of the CV curve did not change as the scan rate increased, and it continued to exhibit a fast and reversible redox property, demonstrating that the electrode material can achieve a rapid exchange of electrons and ions on its surface and has good stability. Due to the neutralization reaction of some electrolytes during the reaction and the internal resistance brought on by the polarization of the electrode material itself, the oxidation peak tends to be greater and the reduction

peak tends to be smaller as the scan rate rises [39]. As can be seen from Figure 7b, the redox peak of the $\text{Nd}_2\text{O}_3/\text{Co}_3\text{O}_4/\text{NF}$ electrode is lower than that of the $\text{Nd}_2\text{O}_3/\text{Co}_3\text{O}_4/\text{rGO}/\text{NF}$ electrode. This, together with the latter morphological composition, suggests that the 3D hierarchical porous spherical honeycomb shape created by the addition of graphene is more conducive to the interaction between the ions in the electrolyte and the electrode material, increasing the active sites and thus accelerating the Faraday redox rate. The electrode material electrochemical properties are drastically improved further. The ion transfer reaction between Nd_2O_3 and Co_3O_4 in a solution of 6 mol/LKOH is described in the following for the CV test [40].



As a result, the valence change of Nd and Co is what is responsible for the redox peaks in the CV curves [41]. Figure 7d displays the constant-current charge/discharge curves of the $\text{Nd}_2\text{O}_3/\text{Co}_3\text{O}_4/\text{rGO}/\text{NF}$ electrode at various current densities with a voltage window of -0.1 to 0.4 V in order to further describe the electrochemical characteristics of the electrode materials. It can also be obtained that only a very small portion of the capacitance of the electrode material is provided by the double-layer since rGO sets up a double-layer capacitance in the electrode material that causes the potential to change accordingly with time but almost flat with the potential axis [42]. This phenomenon demonstrates the pseudo-capacitance of the electrode [43]. When the current density drops to 1A/g , the plateau duration is the longest and the charge/discharge time is also the longest. In the charge/discharge curves, it is noticeable that the slope of the potential versus time is different but there is always a plateau area. The GCD comparison curves of the electrodes consisting of $\text{Nd}_2\text{O}_3/\text{Co}_3\text{O}_4/\text{rGO}/\text{NF}$, $\text{Co}_3\text{O}_4/\text{rGO}/\text{NF}$, and $\text{Nd}_2\text{O}_3/\text{rGO}/\text{NF}$ are shown in Figure 7e when the current density is 1A/g . The following equation provides the qualitative GCD curve computation of the electrode-specific capacitance [44].

$$C = \frac{(I \times \Delta t)}{(m \times \Delta V)} \quad (9)$$

When the current densities are 1, 2, 4, 6, 8, and 10A/g , respectively, the magnitudes of the specific capacitance of the corresponding $\text{Nd}_2\text{O}_3/\text{Co}_3\text{O}_4/\text{rGO}/\text{NF}$ electrodes are 3359.6, 3259.6, 3098.4, 2989.2, 2900.8, and 2828.0F/g , respectively. The magnitudes of the specific capacitance of the $\text{Co}_3\text{O}_4/\text{rGO}/\text{NF}$ electrodes are 2082, 1804.8, 1528.8, 1335.6, 1212.8, and 1100.0F/g , respectively. The specific capacitance values of the $\text{Nd}_2\text{O}_3/\text{rGO}/\text{NF}$ electrodes were 1886, 1776.4, 1681.6, 1612.8, 1563.2, and 1520.0F/g as shown in Figure 7f. It has been demonstrated that when the current density becomes higher, the rate of redox processes occurring on the electrode surface likewise accelerates, and the diffusion rate prevents the loss of ions. As a result, as the current density rises, the specific capacitance of the electrode diminishes [45]. The maximum specific capacitance of the $\text{Nd}_2\text{O}_3/\text{Co}_3\text{O}_4/\text{rGO}/\text{NF}$ electrode may reach 3359.6F/g when the current density is 1A/g , which is 1.61 times more than that of the monometallic $\text{Co}_3\text{O}_4/\text{rGO}/\text{NF}$ electrode (2082F/g) and 1.78 times greater than that of the monometallic $\text{Nd}_2\text{O}_3/\text{rGO}/\text{NF}$ electrode (1886F/g). These results solidify the great ability of the $\text{Nd}_2\text{O}_3/\text{Co}_3\text{O}_4/\text{rGO}/\text{NF}$ composite electrode to optimize electrode structure, increase electrode-specific capacitance size, and enhance electrochemical performance. The monometallic CV and GCD curves of the $\text{Co}_3\text{O}_4/\text{rGO}/\text{NF}$ and $\text{Nd}_2\text{O}_3/\text{rGO}/\text{NF}$ electrodes are depicted in Figure S2. The combination of specific capacitance and Coulomb efficiency at various current densities determines whether this porous spherical electrode material can have remarkable application prospects in the SC area. The specific capacitance of the $\text{Nd}_2\text{O}_3/\text{Co}_3\text{O}_4/\text{rGO}/\text{NF}$ electrode may still acquire 2828.0F/g when the current density

goes up to 10 A/g, as shown in Figure 7f. Despite the decrease in current density, the two electrodes of the symmetric SC composed of this electrode are still able to maintain a high Coulomb efficiency as shown in Figure 7g. The following equation may be employed to identify the electrode Coulomb efficiency [46].

$$\eta = \frac{t_d}{t_c} \times 100\% \quad (10)$$

where the discharge and charging times, respectively, are denoted by t_d (s) and t_c (s) respectively.

This discloses the exceptional reversibility of charging and discharging that this reactive pseudocapacitive material possesses, confirming its excellent electrochemical performance and highlighting the enormous potential of this electrode material for use in the SC area.

Using the electrochemical impedance spectroscopy (EIS) technique, impedance investigations were carried out in a 6 mol/L KOH solution at an open circuit potential from 100 kHz to 0.01 Hz in order to identify the impedance magnitude of the $\text{Nd}_2\text{O}_3/\text{Co}_3\text{O}_4/\text{rGO}/\text{NF}$ electrode. The principal factors that influence the electrode material resistance, according to the fitted equivalent circuit, are the charge transfer resistance (R_{ct}) and diffusion resistance (Warburg impedance). The beginning internal resistance (R_s), which can be derived from the x -axis intercept [47], is mainly composed of the ionic resistance of the electrolyte solution, the intrinsic resistance of the active material, and the contact resistance at the interface between the active material and collector. The R_{ct} decreases as the semicircle becomes more restricted. Smaller Warburg impedances result from steeper slopes. The collected Nyquist curves were compared and analyzed, as shown in Figure 7h. The impedance of the $\text{Nd}_2\text{O}_3/\text{Co}_3\text{O}_4/\text{rGO}/\text{NF}$ electrode increases sharply and more steeply than that of the other electrodes in the low-frequency region [48], inferring a smaller Warburg resistance, which implies a lower electrolyte diffusion resistance and a higher ion diffusion rate of the electrolyte in this electrode material [49]. In the high-frequency region, the R_s values for $\text{Nd}_2\text{O}_3/\text{Co}_3\text{O}_4/\text{rGO}/\text{NF}$, $\text{Co}_3\text{O}_4/\text{rGO}/\text{NF}$, and $\text{Nd}_2\text{O}_3/\text{rGO}/\text{NF}$ are 0.49, 0.65, and 0.52 Ω , respectively. The diameter of the semicircle in the high-frequency region represents the R_{ct} , and the absence of a large semicircle there denotes a very rapid charge transfer rate, which can be related to the fact that the 3D hierarchical porous spherical honeycomb-like structures made of nanoparticles are exceedingly porous. While increasing the permeability of the electrolyte, making it easier to penetrate the electroactive material, and narrowing the ion/electron diffusion path [50]. The shape of a porous spherical honeycomb composed of nanosheets with a high specific surface area offers more electroactive sites for rapid diffusion and movement of ions. By creating a special microspherule-like structure in the area between the nanosheets, which also increases electrical conductivity and electrochemical activity, the space between the nanosheets slows the volume expansion brought on by cyclic charging and discharging.

The experiments were carried out under the conditions of employing $\text{Nd}_2\text{O}_3/\text{Co}_3\text{O}_4/\text{rGO}/\text{NF}$ electrodes as the positive and negative electrodes, filter paper as the septum between the two electrodes, and KOH solution with a concentration of 6 mol/L as the test environment for the assembled symmetrical SC in order to further examine the application prospects of $\text{Nd}_2\text{O}_3/\text{Co}_3\text{O}_4/\text{rGO}/\text{NF}$ electrode materials as supercapacitor electrode materials. Figure 8a depicts the CV curves of the SC while the scan rate (5–100 mV/s) was altered. Based on observation and comparison, it can be inferred that the curves at various scan rates all had a roughly rectangular shape, indicating the good pseudocapacitive performance of the electrode material [51], and that the overall shape did not vary as the scan rate was changed, demonstrating the high rate performance of the SC and the great design. When the scan rate is altered, the overall shape retains the same, evidencing the high rate performance and practical properties of the SC [52]. The GCD curves of the matching SCs are shown in Figure 8b when the current density is altered. All of the GCD curves exhibit prominent triangles, indicating that the $\text{Nd}_2\text{O}_3/\text{Co}_3\text{O}_4/\text{rGO}/\text{NF}$ electrode is in a condition

of rapid ion transport. With the change in current density, the shapes of the triangles do not change considerably, indicating that the SC has high capacitive performance [53]. When the current densities are 0.5, 1, 2, 4, 6, 8, 10, and 20 A/g, the corresponding specific capacitances of 440.4, 400.8, 361, 322, 298, 280, 265,220 F/g are shown in Figure 8c. According to Equations (2) and (3), Figure 8d depicts the link between the energy density and power density of the SC. 30,000 cycles of charge and discharge at a current density of 10 A/g and a voltage window of $-0.6\sim 0.6$ V were measured on the symmetric SC made up of $\text{Nd}_2\text{O}_3/\text{Co}_3\text{O}_4/\text{rGO}/\text{NF}$ electrodes. The capacitor GCD curves for the first 10 cycles are shown in Figure 8e, and the GCD curves for the last 10 cycles as shown in Figure 8f demonstrate that the reaction is still reversible. After 30,000 cycles at a high current density, the capacitance retention rate was still 95.7% as shown in Figure 8g. The stability of the composite electrode material made of $\text{Nd}_2\text{O}_3/\text{Co}_3\text{O}_4/\text{rGO}$ is confirmed by this finding. Through the images, a slight rise in specific capacitance was seen during cycling, which was thought to be caused by the electrode material being activated throughout the constant charging and discharging process, exposing additional active sites. In the efficient cycling stability performance of the super-electricity, the synergistic implications of Nd_2O_3 , Co_3O_4 , and rGO play a key role. The development of in situ voids in the 3D hierarchical porous spherical honeycomb-like structures created on the NF substrate significantly boosts the effective active area in contact with the electrolyte, effectively reduces volume expansion brought on by frequent charging and discharging, and strengthens cycling performance.

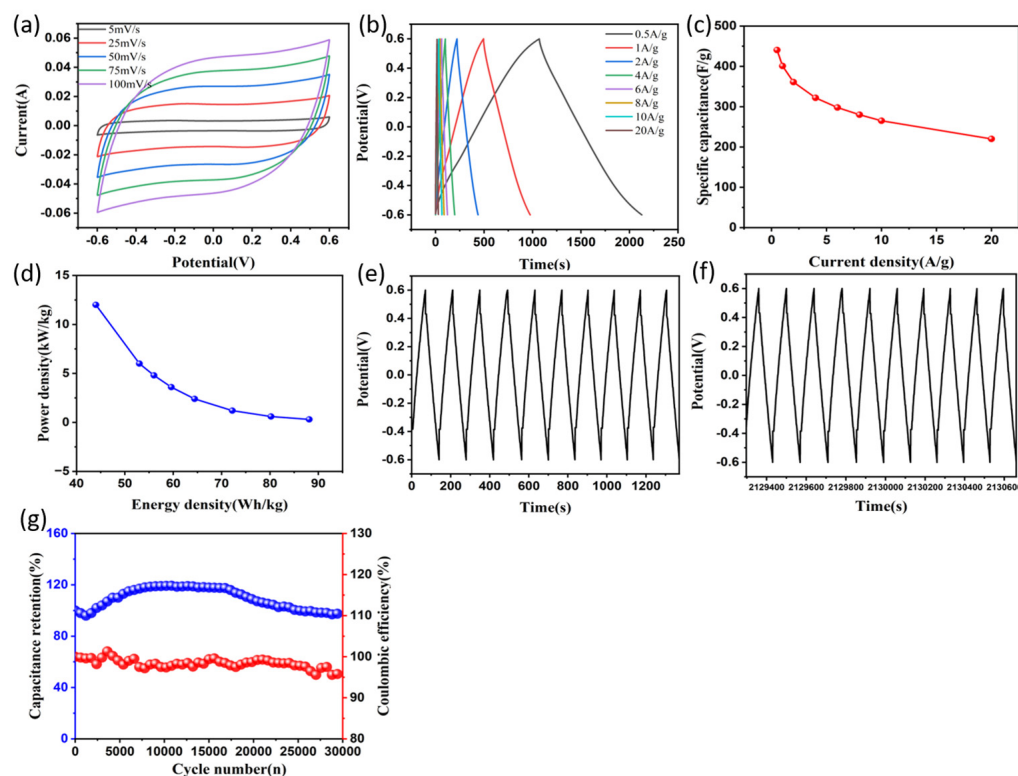


Figure 8. (a) CV curves of the symmetric SC under different scan rates; (b) GCD curves of the SC at different current densities; (c) specific capacitances of the SC at different current densities; (d) Ragone plot related to power and energy densities of the SC; (e,f) the GCD curves for the first 10 cycles and the last 10 cycles out of 30,000 cycles; (g) the capacitance retention and Coulombic efficiency at a current density of 10 A/g for 30,000 cycles; The electrolyte for all the above electrochemical tests was 6 mol/L KOH solution.

Electrochemical impedance spectroscopy (EIS) was employed to verify the materials' properties before and after 30,000 cycles. Figure 9a shows the SC Nyquist curves before and after cycling. With an R_{ct} value of 1.1Ω , which is higher than that of the pre-cycled

material ($R_{ct} = 0.5 \Omega$), the post-cycled material displays a wider radius of arc in the high-frequency band, indicating an increase in charge transfer resistance. Additionally, the slope is lower in the low-frequency range, suggesting a rise in Warburg impedance. All resistance magnitudes, however, are raised properly. After 30,000 cycles at a current density of 10 A/g, Figure 9b displays the SEM pictures of the 3D hierarchical spherical honeycomb-like structures of $\text{Nd}_2\text{O}_3/\text{Co}_3\text{O}_4/\text{rGO}/\text{NF}$. The morphology and structure of the electrode do not change significantly during repeated charging and discharging, with the exception of a small amount of volume expansion and a slight reduction in surface roughness brought on by the redox reaction. The $\text{Nd}_2\text{O}_3/\text{Co}_3\text{O}_4/\text{rGO}/\text{NF}$ electrode may have strong structural stability as a result of this. The Bode phase frequency plots of the supercapacitor before and after cycling are shown in Figure 9c. It can be seen from the curves that the after-cycling curve is a little bit lower than the before-cycling curve, and both phase angles tend to stabilize and approach 0° at the high frequency area. At 100 Hz, the phase angle in the low- and medium-frequency zone starts to progressively grow, and at the limit frequency of 0.01 Hz, the phase angles are -79° and -70.9° , respectively, both exhibiting good capacitance characteristics. The simulated supercapacitor equivalent circuit diagram is shown in Figure 9d. Table 1 displays that the constructed $\text{Nd}_2\text{O}_3/\text{Co}_3\text{O}_4/\text{rGO}/\text{NF}$ electrode has greater performance in all respects when assessing the materials employed in this work with those employed in earlier reports.

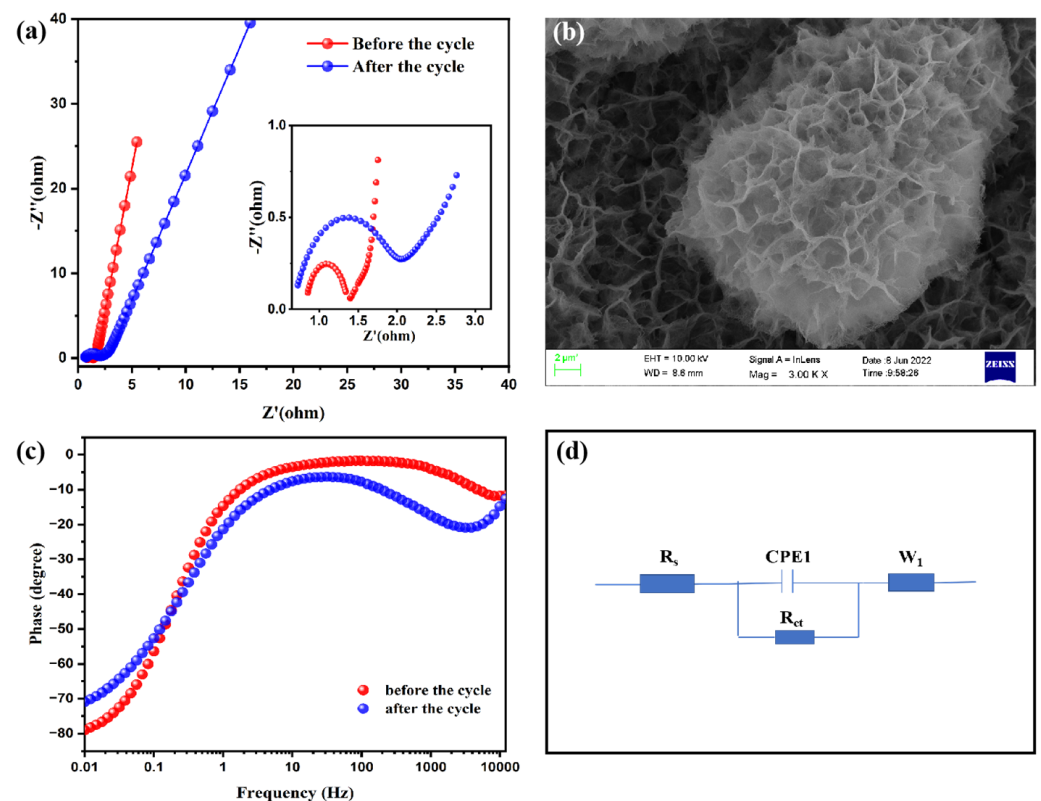


Figure 9. (a) the Nyquist plot of the symmetric SC before and after 30,000 cycles, the inset is the plot in the high-frequency region; (b) SEM image of the symmetric SC after discharging/charging for 30,000 cycles at a current density of 10 A/g. The electrolyte was 6 mol/L KOH solution; (c) Bode phase diagram of the symmetric SC before and after 30,000 cycles; (d) the simulated supercapacitor equivalent circuit diagram.

Table 1. Comparison of electrochemical performances of Nd₂O₃/Co₃O₄/rGO/NF composite electrode in our work with previous reports.

Electrode Materials	Specific Capacitance	Cycling Performance	Energy Density at Power Density	Ref.
Co ₃ O ₄ /rGO composites	1152 F/g at 1 A/g	89.1 % (5000 cycles)	57.26 Wh/kg at 2240.68 W/kg	[54]
CeO ₂ /Co ₃ O ₄ composites	255 F/g at 0.25 A/g	90.1 % (3000 cycles)	27.5 Wh/kg at 500 W/kg	[55]
Nd(OH) ₃ /g-C ₃ N ₄ composites	426.40 F/g at 1A/g	88.3% (3000 cycles)	no data	[56]
Fe ₃ O ₄ /C composites	490.2 F/g at 1A/g	90.7 % (1000 cycles)	34.3 Wh/kg at 1003.9 W/kg	[57]
Nd ₂ O ₃ /Co ₃ O ₄ /rGO/NF	3359.6 F/g at 1A/g	95.7% (30,000 cycles)	88.1 Wh/kg at 300 W/kg	This work

4. Conclusions

The stable composite material of Nd₂O₃, Co₃O₄, and reduced graphene oxide with unique 3D hierarchical porous spherical honeycomb-like structures on nickel foam was successfully prepared using a straightforward one-step hydrothermal synthesis technique coupled with a high-temperature annealing process. The data indicated that the metallic oxides cubic-Nd₂O₃ and cubic-Co₃O₄ efficiently inhibit the aggregation and accumulation of reduced graphene oxide throughout the reaction process, while the specific surface area of Nd₂O₃/Co₃O₄/rGO material up to 107.6246 m²/g with an average pore size of about 12 nm improves the interaction area between the porous microspheres and the electrolyte. Along with its outstanding electrical conductivity, reduced graphene oxide enhances dual capacitance performance in addition to its contribution to electron transport, thereby supplying more energy to the reaction. The Nd₂O₃/Co₃O₄/rGO electrode in the experiment had a specific capacitance of 3359.6 F/g at 1A/g in a 6 M KOH solution. The composite electrodes were assembled into symmetrical supercapacitors and tested electrochemically, the results were remarkable. The capacitance retention rate of 95.7% even at a high current density of 10 A/g after 30,000 continuous charge/discharge cycles, and the specific capacitance reached a maximum of 440.4 F/g at a capacitance density of 0.5 A/g. As well, the energy density is 88.1 Wh/kg at a power density of 300 W/kg. In addition to deriving from the particular porous honeycomb spherical structure of Nd₂O₃/Co₃O₄/rGO, the composite electrode's high electrochemical performance in the three-electrode and two-electrode systems is also directly tied to the synergistic impact between the three. This opens up new opportunities and avenues for the development of rare earth metal oxide Nd₂O₃ as a new kind of Faraday energy storage supercapacitor electrode material.

Supplementary Materials: The following supporting information can be downloaded at: <https://www.mdpi.com/article/10.3390/ma16041694/s1>, S1: Preparation of Nd₂O₃/Co₃O₄/NF composite electrode; S2: Preparation of Nd₂O₃/rGO/NF composite electrode; S3: Preparation of Co₃O₄/rGO/NF composite electrode; S4: Preparation of rGO/NF composite electrode; Figure S1: EDS elemental mapping images of the composite (Nd, Co, Ni, O and C); Figure S2: (a,b) CV curves of Co₃O₄/rGO/NF and Nd₂O₃/rGO/NF electrodes under different scan rates; (c,d) GCD curves of Co₃O₄/rGO/NF and Nd₂O₃/rGO/NF electrodes at different current densities.

Author Contributions: Writing—original draft, H.L.; Data collection and curation, H.L.; writing—review and editing, H.L., S.W. and S.L.; supervision and project administration, M.Z., S.L. and W.X. All authors have read and agreed to the published version of the manuscript.

Funding: We sincerely appreciate the support of the National Natural Science Foundation of China (No. 21271027) for this effort.

Institutional Review Board Statement: Not applicable.

Informed Consent Statement: Not applicable.

Data Availability Statement: Not applicable.

Conflicts of Interest: The authors declare no conflict of interest.

References

1. Fan, P.; Xu, L. Core-Shell Carbon Nanofibers@Ni(OH)₂/NiO Composites for High-Performance Asymmetric Supercapacitors. *Materials* **2022**, *15*, 8377. [[CrossRef](#)] [[PubMed](#)]
2. Shinde, S.K.; Jalak, M.B.; Karade, S.S.; Majumder, S.; Tamboli, M.S.; Truong, N.T.; Maile, N.C.; Kim, D.-Y.; Jagadale, A.D.; Yadav, H.M. A Novel Synthesized 1D Nanobelt-like Cobalt Phosphate Electrode Material for Excellent Supercapacitor Applications. *Materials* **2022**, *15*, 8235. [[CrossRef](#)] [[PubMed](#)]
3. Conway, B.E.; Birss, V.; Wojtowicz, J. The role and utilization of pseudocapacitance for energy storage by supercapacitors. *J. Power Sources* **1997**, *66*, 1–14. [[CrossRef](#)]
4. Zheng, J.P.; Huang, J.; Jow, T.R. The Limitations of Energy Density for Electrochemical Capacitors. *J. Electrochem. Soc.* **1997**, *144*, 2026. [[CrossRef](#)]
5. Karthikeyan, S.; Narenthiran, B.; Sivanantham, A.; Bhatlu, L.D.; Maridurai, T. Supercapacitor: Evolution and review. *Mater. Today Proc.* **2021**, *46*, 3984–3988. [[CrossRef](#)]
6. Choi, C.; Ashby, D.S.; Butts, D.M.; DeBlock, R.H.; Wei, Q.; Lau, J.; Dunn, B. Achieving high energy density and high power density with pseudocapacitive materials. *Nat. Rev. Mater.* **2020**, *5*, 5–19. [[CrossRef](#)]
7. Chen, S.; Xing, W.; Duan, J.; Hu, X.; Qiao, S.Z. Nanostructured morphology control for efficient supercapacitor electrodes. *J. Mater. Chem. A* **2013**, *1*, 2941–2954. [[CrossRef](#)]
8. Saikia, B.K.; Benoy, S.M.; Bora, M.; Tamuly, J.; Pandey, M.; Bhattacharya, D. A brief review on supercapacitor energy storage devices and utilization of natural carbon resources as their electrode materials. *Fuel* **2020**, *282*, 118796. [[CrossRef](#)]
9. Gu, W.; Yushin, G. Review of nanostructured carbon materials for electrochemical capacitor applications: Advantages and limitations of activated carbon, carbide-derived carbon, zeolite-templated carbon, carbon aerogels, carbon nanotubes, onion-like carbon, and graphene. *Wiley Interdiscip. Rev. Energy Environ.* **2014**, *3*, 424–473. [[CrossRef](#)]
10. Tan, Y.B.; Lee, J.-M. Graphene for supercapacitor applications. *J. Mater. Chem. A* **2013**, *1*, 14814–14843. [[CrossRef](#)]
11. Chen, D.; Wang, Q.; Wang, R.; Shen, G. Ternary oxide nanostructured materials for supercapacitors: A review. *J. Mater. Chem. A* **2015**, *3*, 10158–10173. [[CrossRef](#)]
12. Nandi, D.; Mohan, V.B.; Bhowmick, A.K.; Bhattacharyya, D. Metal/metal oxide decorated graphene synthesis and application as supercapacitor: A review. *J. Mater. Sci.* **2020**, *55*, 6375–6400. [[CrossRef](#)]
13. Wei, C.; Zhang, R.; Zheng, X.; Ru, Q.; Chen, Q.; Cui, C.; Li, G.; Zhang, D. Hierarchical porous NiCo₂O₄/CeO₂ hybrid materials for high performance supercapacitors. *Inorg. Chem. Front.* **2018**, *5*, 3126–3134. [[CrossRef](#)]
14. Liang, S.; Wang, H.; Li, Y.; Qin, H.; Luo, Z.; Huang, B.; Zhao, X.; Zhao, C.; Chen, L. Rare-earth based nanomaterials and their composites as electrode materials for high performance supercapacitors: A review. *Sustainable Energy Fuels* **2020**, *4*, 3825–3847. [[CrossRef](#)]
15. Kai, T.; Ye, T. Magnetic characterization of rare-earth oxide nanoparticles. *Appl. Phys. Lett.* **2020**, *117*, 122410. [[CrossRef](#)]
16. Arunachalam, S.; Kirubasankar, B.; Rajagounder Nagarajan, E.; Vellasamy, D.; Angaiah, S. A Facile Chemical Precipitation Method for the Synthesis of Nd(OH)₃ and La(OH)₃ Nanopowders and their Supercapacitor Performances. *ChemistrySelect* **2018**, *3*, 12719–12724. [[CrossRef](#)]
17. Rezanezhad, A.; Rezaie, E.; Ghadimi, L.S.; Hajalilou, A.; Abouzari-Lotf, E.; Arsalani, N. Outstanding supercapacitor performance of Nd–Mn co-doped perovskite LaFeO₃@nitrogen-doped graphene oxide nanocomposites. *Electrochim. Acta* **2020**, *335*, 135699. [[CrossRef](#)]
18. Theerthagiri, J.; Durai, G.; Tatarchuk, T.; Sumathi, M.; Kuppasami, P.; Qin, J.; Choi, M.Y. Synthesis of hierarchical structured rare earth metal-doped Co₃O₄ by polymer combustion method for high performance electrochemical supercapacitor electrode materials. *Ionics* **2020**, *26*, 2051–2061. [[CrossRef](#)]
19. Kovtyukhova, N.I.; Ollivier, P.J.; Martin, B.R.; Mallouk, T.E.; Chizhik, S.A.; Buzaneva, E.V.; Gorchinskiy, A.D. Layer-by-Layer Assembly of Ultrathin Composite Films from Micron-Sized Graphite Oxide Sheets and Polycations. *Chem. Mater.* **1999**, *11*, 771–778. [[CrossRef](#)]
20. Tyler, S.M.; Narendra, K.; Wang, X.; David, P.; Patrice, S.; Yury, G. Energy Storage Data Reporting in Perspective—Guidelines for Interpreting the Performance of Electrochemical Energy Storage Systems. *Adv. Energy Mater.* **2019**, *9*, 1902007. [[CrossRef](#)]
21. Wang, X.; Xiao, Y.; Su, D.; Zhou, L.; Wu, S.; Han, L.; Fang, S.; Cao, S. High-quality Porous Cobalt Monoxide Nanowires @ Ultrathin Manganese dioxide Sheets Core-Shell Nanowire Arrays on Ni Foam for High-Performance Supercapacitor. *Electrochim. Acta* **2016**, *194*, 376–384. [[CrossRef](#)]
22. Li, R.; Wang, S.; Huang, Z.; Lu, F.; He, T. NiCo₂S₄@Co(OH)₂ core-shell nanotube arrays in situ grown on Ni foam for high performances asymmetric supercapacitors. *J. Power Sources* **2016**, *312*, 156–164. [[CrossRef](#)]
23. Chodankar, N.R.; Dubal, D.P.; Ji, S.-H.; Kim, D.-H. Superfast Electrodeposition of Newly Developed RuCo₂O₄ Nanobelts over Low-Cost Stainless Steel Mesh for High-Performance Aqueous Supercapacitor. *Adv. Mater. Interfaces* **2018**, *5*, 1800283. [[CrossRef](#)]
24. Pan, T.-M.; Lu, C.-H. Response to “Comment on ‘Forming-free resistive switching in Nd₂O₃, Dy₂O₃, and Er₂O₃ films fabricated in full room temperature’”. *Appl. Phys. Lett.* **2012**, *100*, 076102. [[CrossRef](#)]

25. Murugalakshmi, M.; Karunamoorthy, S.; Min, P.C.; Velluchamy, M. Efficient photocatalytic degradation of sulfasalazine and reduction of hexavalent chromium over robust $\text{In}_2\text{S}_3/\text{Nd}_2\text{O}_3$ heterojunction under visible light. *J. Water Process Eng.* **2022**, *45*, 102492. [[CrossRef](#)]
26. Li, J.; Zou, P.-c.; Yao, W.-t.; Liu, P.; Kang, F.-y.; Yang, C. An asymmetric supercapacitor based on a $\text{NiO}/\text{Co}_3\text{O}_4/\text{NiCo}$ cathode and an activated carbon anode. *New Carbon Mater.* **2020**, *35*, 112–120. [[CrossRef](#)]
27. Tatsumi, K.; Tsutsui, M.; Beall, G.W.; Mullica, D.F.; Milligan, W.O. Satellite phenomena in the X-ray photoelectron spectra of lanthanide trihydroxides. *J. Electron Spectrosc. Relat. Phenom.* **1979**, *16*, 113–118. [[CrossRef](#)]
28. Zhang, X.H.; Huang, J.M.; Tian, Y.B.; Ye, C.M.; Yang, S.H. Electrochemical Reduction Mechanism of Nd (III) in NaCl-KCl-NdCl_3 Molten Salt on Tungsten. *Electrode Chinese Rare Earths* **2022**, *43*, 82–89. [[CrossRef](#)]
29. Jeon, H.; Han, J.H.; Yu, D.M.; Lee, J.Y.; Kim, T.-H.; Hong, Y.T. Synthesis of mesoporous reduced graphene oxide by Zn particles for electrodes of supercapacitor in ionic liquid electrolyte. *J. Ind. Eng. Chem.* **2017**, *45*, 105–110. [[CrossRef](#)]
30. Li, X.; Liu, Y.; Guo, W.; Chen, J.; He, W.; Peng, F. Synthesis of spherical PANI particles via chemical polymerization in ionic liquid for high-performance supercapacitors. *Electrochim. Acta* **2014**, *135*, 550–557. [[CrossRef](#)]
31. Guo, H.; Wang, X.; Qian, Q.; Wang, F.; Xia, X. A green approach to the synthesis of graphene nanosheets. *ACS nano* **2009**, *3*, 2653–2659. [[CrossRef](#)] [[PubMed](#)]
32. Yao, Z.; Zhu, M.; Jiang, F.; Du, Y.; Wang, C.; Yang, P. Highly efficient electrocatalytic performance based on Pt nanoflowers modified reduced graphene oxide/carbon cloth electrode. *J. Mater. Chem.* **2012**, *22*, 13707. [[CrossRef](#)]
33. Zhu, M.; Dong, Y.; Xiao, B.; Du, Y.; Wang, X. Enhanced photocatalytic hydrogen evolution performance based on Rutrisdicarboxybipyridine-reduced graphene oxide hybrid. *J. Mater. Chem.* **2012**, *22*, 23773–23779. [[CrossRef](#)]
34. Patel, S.; Dhak, P.; Kim, M.K.; Lee, J.H.; Kim, S.K. Structural and magnetic properties of Co-doped Gd_2O_3 nanorods. *J. Magn. Mater.* **2015**, *403*, 155–160. [[CrossRef](#)]
35. Gao, G.; Wu, H.B.; Dong, B.; Ding, S.; Lou, X.W. Growth of Ultrathin ZnCo_2O_4 Nanosheets on Reduced Graphene Oxide with Enhanced Lithium Storage Properties. *Adv. Sci.* **2015**, *2*, 1400014. [[CrossRef](#)] [[PubMed](#)]
36. Zhai, T.; Wan, L.; Sun, S.; Chen, Q.; Sun, J.; Xia, Q.; Xia, H. Phosphate Ion Functionalized Co_3O_4 Ultrathin Nanosheets with Greatly Improved Surface Reactivity for High Performance Pseudocapacitors. *Adv. Mater.* **2017**, *29*, 1604167. [[CrossRef](#)]
37. Wang, T.; Zhang, H.; Luo, H.; He, M.; Wang, W.; Dai, Y. Controlled synthesis of NiCo_2O_4 nanowires and nanosheets on reduced graphene oxide nanosheets for supercapacitors. *J. Solid State Electrochem.* **2015**, *19*, 3309–3317. [[CrossRef](#)]
38. Cao, Y.; Lin, B.; Sun, Y.; Yang, H.; Zhang, X. Structure, morphology and electrochemical properties of $\text{La}_x\text{Sr}_{1-x}\text{Co}_{0.1}\text{Mn}_{0.9}\text{O}_{3-\delta}$ perovskite nanofibers prepared by electrospinning method. *J. Alloys Compd.* **2015**, *624*, 31–39. [[CrossRef](#)]
39. Babu, I.M.; William, J.J.; Muralidharan, G. Surfactant tuned morphology of mesoporous $\beta\text{-Co}(\text{OH})_2/\text{CMC}$ nanoflakes: A prospective candidate for supercapacitors. *J. Solid State Electrochem.* **2019**, *23*, 1325–1338. [[CrossRef](#)]
40. Bailmare, D.B.; Tripathi, P.; Deshmukh, A.D.; Gupta, B.K. Designing of two dimensional lanthanum cobalt hydroxide engineered high performance supercapacitor for longer stability under redox active electrolyte. *Sci. Rep.* **2022**, *12*, 3084. [[CrossRef](#)]
41. Saleh Ghadimi, L.; Arsalani, N.; Ahadzadeh, I.; Hajalilou, A.; Abouzari-Lotf, E. Effect of synthesis route on the electrochemical performance of CoMnFeO_4 nanoparticles as a novel supercapacitor electrode material. *Appl. Surf. Sci.* **2019**, *494*, 440–451. [[CrossRef](#)]
42. Goljanian Tabrizi, A.; Arsalani, N.; Mohammadi, A.; Namazi, H.; Saleh Ghadimi, L.; Ahadzadeh, I. Facile synthesis of a $\text{MnFe}_2\text{O}_4/\text{rGO}$ nanocomposite for an ultra-stable symmetric supercapacitor. *New J. Chem.* **2017**, *41*, 4974–4984. [[CrossRef](#)]
43. Zhao, C.; Ju, P.; Wang, S.; Zhang, Y.; Min, S.; Qian, X. One-step hydrothermal preparation of $\text{TiO}_2/\text{RGO}/\text{Ni}(\text{OH})_2/\text{NF}$ electrode with high performance for supercapacitors. *Electrochim. Acta* **2016**, *218*, 216–227. [[CrossRef](#)]
44. Mohammadi, A.; Arsalani, N.; Tabrizi, A.G.; Moosavifard, S.E.; Naqshbandi, Z.; Ghadimi, L.S. Engineering rGO-CNT wrapped Co_3S_4 nanocomposites for high-performance asymmetric supercapacitors. *Chem. Eng. J.* **2018**, *334*, 66–80. [[CrossRef](#)]
45. Yuan, C.; Li, J.; Hou, L.; Zhang, X.; Shen, L.; Lou, X. Ultrathin Mesoporous NiCo_2O_4 Nanosheets Supported on Ni Foam as Advanced Electrodes for Supercapacitors. *Adv. Funct. Mater.* **2012**, *22*, 4592–4597. [[CrossRef](#)]
46. Arunachalam, S.; Kirubasankar, B.; Pan, D.; Liu, H.; Yan, C.; Guo, Z.; Angaiah, S. Research progress in rare earths and their composites based electrode materials for supercapacitors. *Green Energy Environ.* **2020**, *5*, 259–273. [[CrossRef](#)]
47. Shi, D.; Zhang, L.; Yin, X.; Huang, T.J.; Gong, H. A one step processed advanced interwoven architecture of $\text{Ni}(\text{OH})_2$ and Cu nanosheets with ultrahigh supercapacitor performance. *J. Mater. Chem. A* **2016**, *4*, 12144–12151. [[CrossRef](#)]
48. Zhang, Q.; Liu, Z.; Zhao, B.; Yong, C.; Zhang, L.; Wu, H.H.; Wang, M.S.; Dai, S.; Zhang, K.; Dong, D. Design and understanding of dendritic mixed-metal hydroxide carbon nanotube array electrode for high-performance asymmetric supercapacitors. *Energy Storage Mater.* **2019**, *16*, 632–645. [[CrossRef](#)]
49. Lv, A.; Lu, S.; Xu, W.; Wang, Z.; Shen, Y.; Liu, G. One-pot synthesis of $\text{NiCo}_2\text{O}_4/\text{rGO}/\text{NF}$ hybrid electrode materials realizing ultrahigh capacitance and rapid charge/discharge at large current density. *Appl. Surf. Sci.* **2020**, *511*, 145538. [[CrossRef](#)]
50. Sivakumar, P.; Jana, M.; Jung, M.G.; Gedanken, A.; Park, H.S. Hexagonal plate-like Ni-Co-Mn hydroxide nanostructures to achieve high energy density of hybrid supercapacitors. *J. Mater. Chem. A* **2019**, *7*, 11362–11369. [[CrossRef](#)]
51. Rakhi, R.B.; Chen, W.; Cha, D.; Alshareef, H.N. Substrate dependent self-organization of mesoporous cobalt oxide nanowires with remarkable pseudocapacitance. *Nano Lett.* **2012**, *12*, 2559–2567. [[CrossRef](#)]

52. Cheng, S.; Shi, T.; Huang, Y.; Tao, X.; Li, J.; Cheng, C.; Liao, G.; Tang, Z. Rational design of nickel cobalt sulfide/oxide core-shell nanocolumn arrays for high-performance flexible all-solid-state asymmetric supercapacitors. *Ceram. Int.* **2017**, *43*, 2155–2164. [[CrossRef](#)]
53. Hui, K.N.; Hui, K.S.; Tang, Z.; Jadhav, V.V.; Xia, Q.X. Hierarchical chestnut-like MnCo_2O_4 nanoneedles grown on nickel foam as binder-free electrode for high energy density asymmetric supercapacitors. *J. Power Sources* **2016**, *330*, 195–203. [[CrossRef](#)]
54. Singh, A.; Akhtar, M.A.; Chandra, A. Trade-off between capacitance and cycling at elevated temperatures in redox additive aqueous electrolyte based high performance asymmetric supercapacitors. *Electrochim. Acta* **2017**, *229*, 291–298. [[CrossRef](#)]
55. Zhu, S.J.; Jia, J.Q.; Wang, T.; Zhao, D.; Yang, J.; Dong, F.; Shang, Z.G.; Zhang, Y.X. Rational design of octahedron and nanowire $\text{CeO}_2@ \text{MnO}_2$ core-shell heterostructures with outstanding rate capability for asymmetric supercapacitors. *Chem. Commun.* **2015**, *51*, 14840–14843. [[CrossRef](#)] [[PubMed](#)]
56. Vivek, E.; Arulraj, A.; Krishnan, S.G.; Khalid, M.; Potheher, V. Novel Nanostructured $\text{Nd}(\text{OH})_3/\text{g-C}_3\text{N}_4$ Nanocomposites (Nanorolls Anchored on Nanosheets) as Reliable Electrode Material for Supercapacitors. *Energy Fuels* **2021**, *35*, 15205–15212. [[CrossRef](#)]
57. Lan, J.; Hou, H.; Liu, X.; Yu, X.; Rong, J.; Chen, F. Hierarchical dumbbell-like $\text{Fe}_3\text{O}_4/\text{C}$ electrode for the supercapacitor. *Mater. Lett.* **2023**, *331*, 133302. [[CrossRef](#)]

Disclaimer/Publisher's Note: The statements, opinions and data contained in all publications are solely those of the individual author(s) and contributor(s) and not of MDPI and/or the editor(s). MDPI and/or the editor(s) disclaim responsibility for any injury to people or property resulting from any ideas, methods, instructions or products referred to in the content.